

Prospects of low-dimensional and nanostructured silicon-based thermoelectric materials: Findings from theory and simulation

Neophytos Neophytou

School of Engineering, University of Warwick, Coventry, CV4 7AL, UK

e-mail: N.Neophytou@warwick.ac.uk

Abstract

Silicon based low-dimensional materials receive significant attention as new generation thermoelectric materials after they have demonstrated record low thermal conductivities. Very few works to-date, however, report significant advances with regards to the power factor. In this review we examine possibilities of power factor enhancement in: i) low-dimensional Si channels and ii) nanocrystalline Si materials. For low-D channels we use atomistic simulations and consider ultra-narrow Si nanowires and ultra-thin Si layers of feature sizes below 15nm. Room temperature is exclusively considered. We show that, in general, low-dimensionality does not offer possibilities for power factor improvement, because although the Seebeck coefficient could slightly increase, the conductivity inevitably degrades at a much larger extent. The power factor in these channels, however, can be optimized by proper choice of geometrical parameters such as the transport orientation, confinement orientation, and confinement length scale. Our simulations show that in the case where room temperature thermal conductivities as low as $\kappa_1=2$ W/mK are achieved, the ZT figure of merit of an optimized Si low-dimensional channel could reach values around unity. For the second case of materials, we show that by making effective use of energy filtering, and taking advantage of the inhomogeneity within the nanocrystalline geometry, the underlying potential profile and dopant distribution, large improvements in the thermoelectric power factor can be achieved. The paper is intended to be a review of the main findings with regards to the thermoelectric performance of nanoscale Si through our simulation work as well as through recent experimental observations.

Index terms: low-dimensional silicon, nanowires, ultra-thin layers, thermoelectricity, thermoelectric power factor, Seebeck coefficient, thermal conductivity, atomistic calculations, Boltzmann transport.

I. Introduction

The ability of a material to convert heat into electricity is measured by the dimensionless figure of merit $ZT = \sigma S^2 T / (\kappa_e + \kappa_l)$, where σ is the electrical conductivity, S is the Seebeck coefficient, and κ_e and κ_l are the electronic and lattice parts of the thermal conductivity, respectively. Low-dimensional semiconductor nanostructures are promising candidates for next generation thermoelectric (TE) applications because of their extremely low thermal conductivities compared to those of their corresponding bulk material, and therefore large figures of merit. Silicon, the most common semiconductor with the most advanced industrial processes, is a poor TE material with room temperature $ZT_{bulk} \sim 0.01$, a result of its high thermal conductivity $\kappa_l \sim 140 \text{ W/mK}$.

Silicon nanostructures, on the other hand, have demonstrated a significantly higher $ZT \sim 0.5$ [1, 2, 3, 4], and they are now considered as emerging candidates for high efficiency and large volume production TE applications [5]. This large performance improvement was a result of a drastic reduction in the Si nanostructures' thermal conductivity to values down to $\kappa_l = 1-2 \text{ W/mK}$, close to the amorphous limit [1, 2, 4, 6, 7, 8, 9]. It has very recently become evident, however, that benefits from κ_l reduction are reaching their limits, and further increases of ZT can only be achieved through improvements in the power factor σS^2 [5, 10]. By nanostructuring, the electronic structure could be engineered to tune the Seebeck coefficient [11, 12, 13] and the electrical conductivity independently [14, 15], which could maximize σS^2 . Hicks and Dresselhaus suggested that the sharp features in the low-dimensional density of states function $DOS(E)$ can improve the Seebeck coefficient [11, 12]. Mahan and Sofo have further shown that thermoelectric energy conversion through a single energy level (0D channel) can reach the Carnot efficiency when κ_l is zero [16]. Despite large efforts by the TE community over the last several years, however, it was not possible to successfully demonstrate benefits from low-dimensionality effects on the TE power factor of materials. The adverse interplay between the Seebeck coefficient and electrical conductivity seems to be more complicated than initially anticipated, also depending on the energy dependence of the scattering mechanisms.

In this review paper, we present a summary of our main theoretical efforts to increase the TE power factor in Si-based low-dimensional and nanostructured materials. Using simplified arguments, we explicitly show that the shape of low-dimensional *DOS* alone does not provide significant benefits to the thermopower or to the thermoelectric power factor. We then compute the thermoelectric power factor for 2D Si ultra-thin-layers (UTLs) and 1D Si nanowires (NWs) as shown in Fig. 1a and 1b, respectively, using atomistic calculations and Boltzmann transport. We demonstrate that in these channels the electrical conductivity is degraded in such a way due to enhanced electron-phonon and electron-surface roughness scattering (SRS), that the power factor is dramatically reduced. We identify, however, optimization directions using geometrical features such as the transport and confinement orientations (see Fig. 1a, 1b) to achieve the highest possible power factor, and illustrate the design principles behind this. For this analysis, we employ the atomistic $sp^3d^5s^*$ -spin-orbit-coupled ($sp^3d^5s^*$ -SO) tight-binding (TB) model [17, 18, 19, 20, 21, 22, 23] coupled to Linearized Boltzmann transport as described in Refs. [14, 24, 25]. Considering the full atomistic nature is necessary to properly address the properties of nanoscale Si channels. Using literature data for the thermal conductivity of Si nanostructures we extract the *ZT* figure of merit, showing that room temperature values of $ZT \sim 1$ can indeed be achieved, in agreement with experimental data.

In the second part of the paper, we discuss the thermoelectric potential of 3D Si-based nanostructured materials. First, we describe the performance of nanocrystalline Si material as shown in the schematic of Fig. 1c. We describe how a carefully designed Si nanograin geometry, with a carefully designed underlying potential distribution and dopant distribution, can make effective use of energy filtering and structure inhomogeneities, and provide large TE power factors, even up to $\sim 5\times$ higher compared to bulk Si. We present simple explanations for this behavior, backed by recent experimental observations [26, 27]. We then discuss the prospect of Si nanomeshes (or nanoporous Si) and Si-based heterostructures for TE applications.

The paper is organized as follows: In Section II we explain the influence of low-dimensionality on the thermoelectric coefficients in general, and for Si in particular. In Section III we present an analysis for the TE properties of Si ultra-thin-layers (UTLs) and nanowires (NWs). In Section IV we discuss the TE potential Si-based nanostructured materials, and finally in Section V we conclude.

II. Thermoelectric coefficients in low-dimensional materials

Here we consider the TE coefficients of n-type Si materials. The electrical conductivity σ and the Seebeck coefficient S are computed within the linearized Boltzmann transport equation (BTE) theory as:

$$\sigma = q_0^2 \int_{E_C}^{\infty} dE \left(-\frac{\partial f_0}{\partial E} \right) \Xi(E), \quad (1a)$$

$$S = \frac{q_0 k_B}{\sigma} \int_{E_C}^{\infty} dE \left(-\frac{\partial f_0}{\partial E} \right) \Xi(E) \left(\frac{E - E_F}{k_B T} \right), \quad (1b)$$

where the transport distribution function $\Xi(E)$ is defined as [25]:

$$\begin{aligned} \Xi(E) &= \frac{1}{W} \sum_{k_{x,y},n} v_{x,n}^2(k_{x,y}) \tau_n(k_{x,y}) \delta(E - E_n(k_{x,y})) \\ &= \frac{1}{W} \sum_n v_{x,n}^2(E) \tau_n(E) g_{2D}^n(E). \end{aligned} \quad (2)$$

Here $v_{x,n}(E) = \frac{1}{\hbar} \frac{\partial E_n}{\partial k_x}$ is the group velocity in the transport direction (extracted from the curvature of the bands for each subband n and momentum $k_{x,y}$), $\tau_n(k_{x,y})$ is the momentum relaxation time of a carrier with in-plane wave number $k_{x,y}$ in subband n , $g_{2D}^n(E_n)$ is the density of states for a 2D subband, E_C is the conduction band edge, W is the thickness of the channel, and E_F is the Fermi level, determined by the doping of the material. Note that the above expressions are relevant for a 2D ultra-thin layer channel extending in the (x, y) direction, where x - is the transport direction and the z -direction is confined. In the case of 1D channels, i.e. NWs, the y -index drops out, and the width of

the channel W becomes the cross sectional area A . The complete formalism is described in [14], where the relaxation times and for phonons are given by the following expressions:

$$\frac{1}{\tau_{ph}^n(E)} = \frac{\pi}{\hbar} \frac{\left(N_\omega + \frac{1}{2} \mp \frac{1}{2}\right)}{\rho \hbar \omega_{ph}} \times \left(\frac{1}{L_x L_y} \sum_{m, k_x, y} \frac{|K_{\bar{q}}|^2}{L_{nm}^{k_x, k_x, y}} \delta_{k_x, y', k_x, y \pm q_x, y} \delta(E_m(k_{x, y}') - E_n(k_{x, y}) \pm \hbar \omega_{ph}) \left(1 - \frac{v_m^x(k_{x, y}')}{v_n^x(k_{x, y})}\right) \right), \quad (3)$$

where $\hbar \omega_{ph}$ is the phonon energy, ρ is the mass density of Si, and N_ω is the number of phonons given by the Bose-Einstein distribution. For optical deformation potential scattering it holds $|K_{\bar{q}}|^2 = D_0^2$, whereas for acoustic deformation potential scattering it holds $|K_{\bar{q}}|^2 = q^2 D_{ADP}^2$, where D_0 and D_{ADP} are the scattering deformation potential amplitudes. Specifically for elastic acoustic deformation potential scattering (ADP), after applying the equipartition approximation, the relaxation rate becomes:

$$\frac{1}{\tau_{ADP}^n(E)} = \frac{2\pi}{\hbar} \frac{D_{ADP}^2 k_B T}{\rho v_s^2} \left(\frac{1}{L_x L_y} \sum_{m, k_x} \frac{1}{L_{nm}^{k_x, y, k_x, y'}} \delta_{k_x, y', k_x, y \pm q_x, y} \delta(E_m(k_{x, y}') - E_n(k_{x, y})) \left(1 - \frac{v_m^x(k_{x, y}')}{v_n^x(k_{x, y})}\right) \right), \quad (4)$$

where v_s is the sound velocity in Si. In the expressions above, the quantities in the right-hand-side are all k -resolved when computed from the electronic structure $E(k)$, whereas the scattering rate in the left-hand-side is a function of energy. The δ -functions in Eq. (3) and Eq. (4) state energy conservation. Numerically, the $E(k)$ relation needs to be discretized in energy. All states are sorted in energy and at a particular energy, arrays with all relevant k -states from all subbands are constructed. Note the inverse dependence on the scattering rates to $L_{nm}^{k_x, y, k_x, y'}$, which is proportional to the width of the quantum well L . This is the wavefunction overlap, which decreases as the cross section width is reduced, and correspondingly the electron-phonon scattering rates increase.

Before the thermoelectric coefficients of low-dimensional channels are investigated using computationally expensive atomistic tight-binding simulations, a simplified method is considered to get a first order indication on the effect of low-dimensionality. If one considers a material with single parabolic band, then the bandstructure velocity reduces to a simple $\sim E$ dependence, and the density of states is proportional to $E^{1/2}$, E^0 , and $E^{-1/2}$ for 3D, 2D, and 1D materials respectively. The $DOS(E)$ function for 3D and 1D single parabolic band channels is shown in the inset of Fig. 2 and given, respectively by:

$$g_{3D}(E) = \frac{1}{2\pi^2} \left(\frac{2m^*}{\hbar^2} \right)^{3/2} \tilde{E}^{1/2}, \quad (5)$$

$$g_{1D}(E) = \frac{1}{\pi} \left(\frac{2m^*}{\hbar^2} \right)^{1/2} \tilde{E}^{-1/2}. \quad (6)$$

where $\tilde{E} = E - E_C$. To get an indication for the effect of dimensionality on the Seebeck coefficient, at this point we consider a constant scattering relaxation time τ . By substituting this in Eq. 2 and then Eq. 1b, and using $v_n(E) \propto \sqrt{\tilde{E}/m_{eff}}$, the Seebeck coefficient can be shown to follow [15]:

$$S \propto \frac{\int_{E_C}^{\infty} F(\eta_F) \left(\frac{E - E_F}{k_B T} \right) dE}{\int_{E_C}^{\infty} F(\eta_F) dE} \quad (7)$$

where $F(\eta_F) = \tilde{E}^{d/2} \left(-\frac{\partial f(E - E_F)}{\partial E} \right)$, with d is the dimensionality of the channel. The Seebeck coefficient, therefore, is at first order independent of bandstructure ($F(\eta_F)$ is just a function of energy), and decreases linearly as the energy deviates from the Fermi level as expected ($F(\eta_F)$ is found in both numerator and denominator).

The Seebeck coefficient for 3D and 1D materials versus $\eta_F = E_C - E_F$ (the distance of the Fermi level E_F to the conduction band edge E_C) is shown in Fig. 2. It is evident from here that the Seebeck coefficient degrades for lower dimensionality, an indication that the

low-dimensional shape of the $DOS(E)$ function itself (insets of Fig. 2) is not helpful to the Seebeck coefficient. This was previously discussed by Kim *et al* in Ref. [Kim09], who also pointed out that even if one considers ballistic transport, or energy dependent relaxation times, the conclusions about the Seebeck coefficient do not change because the Seebeck coefficient is at first order independent of scattering as well [28].

A simple explanation as to why the 1D or 2D shape of the DOS energy function is not helpful to the Seebeck coefficient, is that for the Seebeck coefficient to increase one requires a continuously increasing $DOS(E)$ function as the energy increases. This ensures that there are many more states to be filled by hot carriers rather than cold carriers. The $DOS(E)$ function in the case of 1D channels has a singularity at the band edge, resulting in a large increase, but for higher energies the $DOS(E)$ function decreases, providing less and less available states for high energy carriers. The 2D $DOS(E)$ remains constant, and only the 3D $DOS(E)$ function continuously increases as the energy increases, which justifies why the Seebeck is higher for 3D bandstructures.

An increase in the Seebeck coefficient, however, can be indeed observed as a material is scaled down to lower dimensions when one compares the 3D and 1D channels at a fixed carrier density. This is illustrated in Fig. 3. From Eq. 1b and Eq. 7, it can easily be deduced that the Seebeck coefficient is at first order proportional to the distance of the bands from the Fermi level, $\eta_F = E_C - E_F$. Figure 3a shows the bandstructure for a Si NW of diameter $D=12\text{nm}$, calculated using the 20 orbital atomistic tight-binding $sp^3d^5s^*$ -spin-orbit-coupled model [17]. The position of the Fermi level assuming an underlying carrier density of $n=10^{19}/\text{cm}^3$ is indicated by the red line. Figure 3b shows how η_F changes as the diameter of the NW is reduced even further down to $D=3\text{nm}$, towards a truly 1D Si channel. The increase in the η_F indicates that at the same carrier density, the bands move further away from the Fermi level. This can be understood by the fact that a 1D channel consists of several 1D subbands. As the NW diameter is reduced, the number of subbands is also reduced. At some small enough confinement length scale (in the case of Si this is below 10nm), a single band remains within the reach of the Fermi distribution. The carrier density can be written as $n=N/A$, where N is the number of carriers and A is the

cross section area. To keep a constant density n (in this case at $10^{19}/\text{cm}^3$) as the A is reduced, the Fermi level needs to shift down with respect to the bands to reduce N and keep the density n constant. This has implications to the Seebeck coefficient, which follows the trend of η_F . This is indicated in Fig. 3c, which shows the Seebeck coefficient for the [100] directed Si NW versus diameter at $n=10^{19}/\text{cm}^3$, calculated using the BTE [14]. An increase of $\sim 2\times$ is observed, similar to the increase in η_F . The increase in η_F , though, affects the electronic conductivity of the NW as well. From Eq. 1 it can be deduced that the conductivity is actually exponentially proportional to the position of E_F , and the further the bands are located away from the Fermi level, the lower the conductivity would be. Indeed, the reduction in the conductivity is much larger, almost $\sim 4X$ as the diameter is reduced as indicated in Fig. 3d (solid line). Alternatively, this reduction can also be understood as an increase the electron-phonon scattering due to an increase in the electron-phonon interaction. If one considers the effect of surface roughness scattering in addition (dashed line in Fig. 3d), then the electronic conductivity drops by $\sim 10\times$, and such a large drop severely degrades the power factor.

It is therefore obvious that at low dimensions bandstructure effects and quantum confinement effects do not favor the power factor in Si channels, despite the fact that the Seebeck coefficient can benefit (but for reasons different to the shape of the $DOS(E)$ function). It turns out though as we will show below, that just by looking at the behavior of the electronic structure of materials under confinement and by calculating η_F , a rough first order guidance as to the degree that the power factor will be affected can be provided. More specifically, Si low-dimensional channels can be optimized with respect to transport orientation, confinement orientation, and confinement length scale, and each of these channels have different bandstructures and properties, which provide optimization directions for the power factor. Below it is shown how two simple features, the η_F and the bandstructure injection velocities can suggest at first order which channel could be beneficial to the power factor.

III. Thermoelectric power factor in ultra-thin Si layers (UTLs) and nanowires (NWs)

The UTL and NW bandstructures are calculated using the 20 orbital atomistic tight-binding $sp^3d^5s^*$ -spin-orbit-coupled model [17, 20, 23], which is sufficiently accurate and inherently includes the effects of different transport and quantization orientations. In references [14, 22, 24] we showed how this model can be employed to compute thermoelectric properties of semiconductor channels and in particular Si channels. We consider infinitely long, uniform, silicon UTLs and NWs in various transport and surface orientations (in the case of UTLs). The surfaces of the channels are assumed to be passivated. The passivation technique details are provided in Refs. [29, 30]. This model is coupled to the Boltzmann transport equation (BTE) as described by Eq. 1, and Eq. 2. The full details of this coupling are described in Ref. [14].

Confined Si channels have a different electronic structure and different electronic properties depending on the geometrical details. This is because each pair of the six energy ellipsoids in the conduction band of Si (as indicated in Fig. 4a) is projected on the 2D k -space plane with different transport, transverse and quantization masses. Figure 4 shows this by plotting examples of the 2D bandstructure of three different channels: i) the (100)/[110] (Fig. 4b), ii) the (110)/[110] (Fig. 4c), and iii) the (111)/[112] channel (Fig. 4d). The dark-blue regions indicate the energy minima, the regions that determine the transport properties, which are projections of the six energy ellipsoids on the 2D plane. The energy landscape looks completely different on each surface, but also in different orientations within the same surface. This indicates that different thermoelectric properties can be expected from each channel, pointing to potential optimization directions.

Indeed, Fig. 5a shows the average ballistic carrier velocity (or injection velocity v_{inj}) of ultra-thin Si layers in different confinement and transport orientations versus the layer thickness [23]. The injection velocity represents the average ‘positive going’ bandstructure group velocity of the carriers. It is calculated by averaging all

bandstructure velocities (or carrier group velocities $v_x(k_{x,y})$ extracted from the curvature of the electronic structure) of all subbands and momentum states in the transport direction over the fermi distribution as:

$$v_{\text{inj}} = \langle v_x^+ \rangle = \frac{\sum_{k_x > 0} v_x(k_{x,y}) f(k_x)}{\sum_{k_x > 0} f(k_x)} \quad (8)$$

This quantity plays a major role in determining the mobility and conductivity of the channel [31]. Although the injection velocity does not appear explicitly in the solution of the BTE (there all states are used one-by-one in the calculation of the transport distribution function without averaging), at first order it determines the relative change to the conductivity as the dimensionality or feature sizes of the material change. Here we show results for layer thickness from $W=15\text{nm}$ down to $W=3\text{nm}$. Two important effects can be identified: i) the different channel geometries are strongly anisotropic with the carrier velocities varying from $v_{\text{inj}} \sim 0.8 \times 10^5 \text{m/s}$ to $v_{\text{inj}} \sim 1.2 \times 10^5 \text{m/s}$ (in the case of p-type channels this is even more severe [25, 31]). As the carrier mobility depends at first order on $\mu \sim v_{\text{inj}}^3$ [31], it can be expected that the transport properties of the different channels will differ significantly. ii) The second observation is that in some cases the carrier velocity increases with confinement, whereas in others it decreases. Confinement is actually beneficial in the case of TE channels because it strongly degrades the thermal conductivity. Choosing a channel in which the electronic properties also improve with confinement is an obvious optimization direction. In Fig. 5b we plot η_F for the (100), (110) and (112) surfaces. As discussed above, this is the quantity that determines the Seebeck coefficient. The carrier density assumed here is $n=10^{19}/\text{cm}^3$, the one required for optimal power factor as we will demonstrate below. Interestingly, only for the (110) surface η_F increases with thickness reduction. In the case of the (112) surface η_F remains almost unchanged, whereas in the case of the (100) channel, η_F decreases. From this figure, one can easily detect that the (100)/[110] channel will have the largest electrical conductivity, but the lower Seebeck coefficient. The (110)/[110] channel on the other hand, will have the lower conductivity, but the highest Seebeck coefficient.

The results for the actual calculations of the TE coefficients of the Si UTLs are shown in Fig. 6. We show the electrical conductivity (Fig. 6a), the Seebeck coefficient (Fig. 6b), and the thermoelectric power factor (Fig. 6c), versus carrier density. The channels under consideration are the (100)/[110] (red lines), (110)/(110) (green lines), and the (112)/[111] channel (black lines), built on the surfaces considered in Fig. 5b above. Results for two channel thicknesses $W=15\text{nm}$ (solid lines) and $W=3\text{nm}$ (dashed lines) are shown. In the calculations at this point we only consider electron-phonon limited scattering, which will provide an upper limit for the power factor. In Fig. 6a it can be observed that the electrical conductivity is reduced as the width of the layer is reduced (solid versus dashed lines). The reason of the reduced conductivity is the enhanced electron-phonon interaction ($\sim W^{-1}$), which increases the scattering rates [32, 33, 34]. A strong anisotropy is also observed for the thinner UTLs with the (100)/[110] channel performing better compared to the other two channels. The conductivity of the $W=3\text{nm}$ (100)/[110] channel does not degrade significantly compared to the $W=15\text{nm}$ channel, a consequence of the increase in the carrier injection velocity with thickness reduction in this channel as shown in Fig. 5a (red line). The conductivity of the other two channels, however, suffers significantly with width reduction. Note that the (100) surface and [110] transport crystallographic orientations are the ones used in Si technology today, and therefore building n-type TE materials on this channel will be convenient.

This trend is reversed when it comes to the Seebeck coefficient shown in Fig. 6b. The Seebeck coefficients of the wider channels overlap over the entire carrier concentration region, as it would have been expected just by looking at the very similar η_F values at the right side of Fig. 5b. For the thinner channels, however, the Seebeck coefficient deviates, and a significant anisotropy is observed. The Seebeck coefficient increases in the $W=3\text{nm}$ (110)/[110] and secondly in the $W=3\text{nm}$ (112)/[111] channels, whereas it reduces in the case of the (100)/[110] channel. Again, this would have been well expected if one observes the behavior of η_F as shown in Fig. 5b at the left side of the figure. A reduction in η_F signifies a reduction in the Seebeck coefficient and vice versa. This is a clear demonstration of how one can use a single quantity, η_F , to predict the behavior of the Seebeck coefficient as a material is scaled into low-dimensions. Thus, the

v_{inj} together with η_F , provide an intuitive explanation on how the thermoelectric coefficients will behave upon channel cross section scaling, without the need to perform expensive transport calculations.

Finally, in Fig. 6c we plot the thermoelectric power factor for the six channels described above. At carrier concentrations of $n \sim 10^{19}/\text{cm}^3$, the power factor peaks at $\sim 8 \text{mW}/\text{mK}^2$, which is significantly high, also reflecting the relatively high power factors of bulk Si. This is the case for the $W=15\text{nm}$ (100)/[110] channel (red-solid line), whereas the power factor of the $W=15\text{nm}$ (110)/[110] channel (green-solid line) is slightly lower, at $\sim 7 \text{mW}/\text{mK}^2$. The (112)/[111] channel, on the other hand, has a lower power of $\sim 5 \text{mW}/\text{mK}^2$. As the width of the channels decreases, however, the power factor drops in all channel cases. In the case of the (100)/[110] channel (red lines) the power factor drops due to the large decrease in the Seebeck coefficient, whereas in the (112)/[111] channel case (black lines) due to the decrease in the electrical conductivity. The (110)/[110] channel (green lines) exhibits a large drop in the conductivity with thickness reduction, but an increase in the Seebeck coefficient as well, which moderates the drop observed in the power factor.

What we would like to mention following this analysis, though, is that one can have a first order indication as to whether scaling a certain material to low-dimensions will be beneficial for the power factor by looking at the behavior of two simple parameters with feature size reduction: i) the carrier injection velocities v_{inj} and ii) the $\eta_F = E_C - E_F$ at a constant carrier concentration. The first determines the electronic conductivity and the second the Seebeck coefficient. These are simple bandstructure parameters and can be extracted without the use of sophisticated transport formalisms. The analysis here was performed for Si, but it is quite generic and could be applied for other materials as well. Of course, what we describe refers to having a single bulk 3D material, with a specific doping, and then this material is scaled to lower dimensions, i.e. the material stays the same, only the dimensionality changes. This is not to be generalized in the cases of changing the bandstructure of a material by alloying, doping [35, 36], or nanostructuring [37], which in some cases very large power factor improvements were

reported. Clearly, the role of the electronic structure is strong, and the role of its particular features and the explicit role of the scattering mechanisms determine the thermoelectric properties. Further studies need to be performed in different materials to see if what the proposed first order indication holds and can be more generalized.

Using the calculated power factor from Fig. 6c, we compute and plot the ZT figure of merit for the channels presented. For the phonon part of the thermal conductivity we use a constant value $\kappa_1=2\text{W/mK}$ for all UTL thicknesses. A variety of thermal conductivity values can be found in the literature regarding the thermal conductivity of low-dimensional Si, both in experimental and theoretical works [4, 6, 7, 8, 9, 38, 39, 40, 41, 42, 43]. The value $\kappa_1=2\text{W/mK}$ is a commonly reported value for Si nanostructures of feature sizes below 50nm, so for simplicity we chose this value for all UTL thicknesses (although it is expected that the $W=15\text{nm}$ layer will have a higher thermal conductivity compared to the $W=3\text{nm}$ layer). This however, will give us an estimate of the upper limit in the ZT figure of merit for Si at room temperature. The ZT is plotted in Fig. 7. The maximum value obtained is slightly below $ZT\sim 0.9$ for the $W=15\text{nm}$ (100)/[110] channel (red-solid line), which is significant for room temperature conditions, and is also in agreement with recent measurements and other theoretical calculations for low-dimensional Si TEs [44, 45]. The $W=3\text{nm}$ channels have maximum ZT figures of merit varying from $ZT\sim 0.3-0.6$. Note that in these calculations, however, we did not include surface roughness scattering (SRS), which could degrade the electronic conductivity severely for the $W=3\text{nm}$ channels, and reduce the ZT . The conductivity of the wider $W=15\text{nm}$ channels would not suffer strongly from SRS and the ZT figure of merit will be retained, but the $W=3\text{nm}$ channels would be affected [25]. It seems, however, that an optimized upper limit for the ZT figure of merit of Si at room temperature is slightly below unity. The influence of SRS will be considered below.

We next perform a similar analysis for 1D Si nanowire channels. The results for this are shown in Fig. 8. We consider the n-type [100] channel and compute the electronic conductivity (Fig. 8a), Seebeck coefficient (Fig. 8b), and ZT figure of merit (Fig. 8c). In this analysis we include surface roughness scattering (SRS) in addition to

phonon scattering in the calculation. We present results for NWs with diameter $D=12\text{nm}$, $D=6\text{nm}$ and $D=3\text{nm}$. From Fig. 8 it is obvious that the conductivity is strongly degraded as the NW diameter is reduced, partly because electron-phonon interaction increases, and partly because SRS becomes stronger. On the other hand, the large reduction in the conductivity is accompanied with a large increase in the Seebeck coefficient for the $D=3\text{nm}$ NW as shown in Fig. 8b. However, this is not enough to provide increased power factors, and the ZT figure of merit remains lower for the $D=3\text{nm}$ NW compared to the larger NW diameters as shown in Fig. 8c. The room temperature ZT of the $D=12\text{nm}$ NW, however, can reach values slightly above unity. Note that in this case we kept the thermal conductivity of all channels constant at $\kappa_l=2\text{W/mK}$ for consistency, although this might very well not be the case as the diameter changes.

In all of the analysis presented above, we have included phonon-limited electronic transport, and in some cases included surface roughness scattering as well. The power factor, though, is shown to maximize at concentrations around $n\sim 10^{19}/\text{cm}^3$, or somewhat higher. At such high carrier concentrations the dominant scattering mechanism that limits electron transport is ionized impurity scattering - IIS (in the usual case of highly doped materials). We have shown in the past that the mobility of carriers can be reduced even up to an order of magnitude compared to phonon-limited transport [32]. Despite the fact that ionized impurity scattering improves the Seebeck coefficient, in general, the power factor is strongly reduced. This is clearly indicated in Fig. 9, which shows the power factor of the [100] Si NW at carrier concentrations $n=10^{19}/\text{cm}^3$ versus the NW diameter. Three different cases are shown: i) the phonon-limited power factor (only electron-phonon scattering considered in the calculation), ii) phonon plus SRS limited results, iii) phonon, plus SRS, plus ionized impurity scattering (IIS) limited results. The phonon-limited conditions provide the highest power factor, only moderately reduced with diameter reduction because of the increase in the electron-phonon coupling. Once SRS is added, although NWs with larger diameters ($\sim 10\text{nm}$) are not affected, significant power factor degradation is observed for NWs with smaller diameters. Ionized impurity scattering, on the other hand, is a scattering mechanism detrimental to the conductivity. At the entire diameter range the power factor decreases by a factor of $>4X$. In general,

this will reduce the ZT figure of merit in nanoscale Si materials by a similar amount. The close to unity ZT calculated earlier would be reduced by a similar amount.

Several recent studies suggested techniques to avoid transport in the presence of IIS have been proposed, such as modulation doping techniques [46, 47], or gating the channel materials [48, 49, 50, 51, 52, 53]. In this way, the high carrier densities can be achieved without the use of direct doping, and the phonon-limited performance would be achieved. An important point we stressed in Ref. [49], is that SRS is not a strong degrading mechanism in channels with feature sizes $>10\text{nm}$, , despite the fact that the gate field tends to shift carriers on the surface. The reason is that the internal electric fields required to achieve charge accumulation are weak (compared to the fields required to achieve inversion layers, for example). Although the charge tends to be pushed towards the surfaces, SRS is still weak. The problem with these techniques, though, is that the benefits can only be achieved in the material regions where the electric field can reach, which can be rather small. In Ref. [49] it was shown that the effects of gating in Si NWs could possibly diminish for NWs with diameters $D>40\text{nm}$. Still, however, Si NWs will need to be scaled well below 40nm in order to achieve the ultra-low $\kappa_l=2\text{W/mK}$ thermal conductivities for required for high TE performance. Thus, the optimal design for low-dimensional Si TEs will require intrinsic channels of diameters/widths $\sim 10\text{nm}-20\text{nm}$ and modulation doping or gating techniques (assuming $\kappa_l=2\text{W/mK}$ can be achieved at those length scales).

IV. Thermoelectric properties of bulk-size nanostructured Si

The analysis up to here considered only low-dimensional Si materials, and mainly focused on the power factor, assuming that low thermal conductivities can be achieved. The main conclusion is that low-dimensionality does not necessarily provide power factor improvements, on the contrary, the largest power factors are observed for the materials with larger feature sizes. In our recent works, however, we showed that very large power factors can be achieved in nanocrystalline bulk-like Si materials [26, 27, 54].

These are two-phase material geometries consisting of grains of diameter $\sim 30\text{nm}$, separated by grain boundaries of thickness $\sim 2\text{nm}$. Significant power factor improvements can be achieved once the underlying nanostructure is properly designed to incorporate three important effects: *i*) Degenerate doping, δ , non-uniformly distributed in the grain region to achieve overall high conductivity; *ii*) Potential barriers around the grain boundary regions to achieve carrier filtering; and *iii*) variation of the thermal conductivity along the path of the electrical current and heat flow, from grain to grain boundary, to improve the Seebeck coefficient. The basic geometry is shown in Fig. 1c. The material is a nanocrystalline p-type Si, initially degenerately doped at concentrations up to the $p=1.2\times 10^{20}/\text{cm}^3$. Upon sequential annealing steps, the overall carrier concentration is reduced down to $p=5.6\times 10^{19}/\text{cm}^3$, but it becomes highly non-uniformly distributed within the material. The grain regions remain extremely heavily doped (condition *i*), whereas the grain boundaries and the regions around them become very lightly doped. As a result, as is the case in polycrystalline Si, potential barriers form around the grain boundary sides which introduce carrier energy filtering (condition *ii*) [27, 55, 56]. A simplified first order description of the potential profile is shown in the inset of Fig. 11. In addition, as the grain boundaries are amorphous in nature, and the grains are crystalline, the thermal conductivity along the material is non-uniform as well (condition *iii*).

Within the grain, the carrier mobility is ionized impurity scattering dominated, especially in the center of the region. Our calculated carrier mobility for p-type Si, including phonon and ionized impurity scattering is shown in Fig. 10a. The calculation is calibrated to measured data from Refs [57, 58, 59]. Around the relevant operating carrier densities (noted in the figure), the mobility does not degrade with carrier density, but it is rather ‘flat’ as indicated in Fig. 10a. Our calculated mean-free-path (MFP) versus energy for scattering at doping densities $p\sim 10^{20}/\text{cm}^3$ is shown in Fig. 10b. The MFP increases with energy, indicating that high energy carriers will scatter less. At this carrier density the Fermi level resides well into the valence band of Si (red line in the inset of Fig. 11), and provides a large amount of conducting carriers (orange-colored region in the inset of Fig. 11). The main advantage of this geometry, thus, is that the overall high conductivity is provided by the high conductivity in the grains, and the overall high Seebeck coefficient

is provided by energy filtering at the grain boundaries. Grain boundaries contribute to Seebeck increase through another mechanism as well, namely the non-homogeneity of the thermal conductivity along the channel. The Seebeck coefficient is a measure of the voltage induced due to a temperature gradient. The Seebeck of regions with low thermal conductivity tend to dominate the overall Seebeck coefficient in composite systems, because most of the temperature drop is located at these regions. In this case the grain boundaries have a very low thermal conductivity due to their amorphous nature. The high Seebeck coefficient associated with them, thus, determines the overall Seebeck. The result is that the power factor in this material largely overpasses the power factor of bulk crystalline Si as shown in Fig. 11. The improvement is quite significant with power factor at $\sim 15 \text{ mW/mK}$ ($\sim 5\times$ larger compared to bulk – compare the red line to the black line in Fig. 11) and is observed both in experimental studies (blue data point in Fig. 11) as well as theoretical works [26, 54]. Furthermore, a more advanced geometry, in which the grain also includes nanometer scale nanovoids achieved even higher power factor, reaching at 22 mW/mK^2 [60]. The higher power factor compared to the nanocrystalline material without the nanovoids is attributed to its higher Seebeck coefficient. Although more work needs to be done to identify the reasons behind this improvement, it is speculated that the nanovoids improve the Seebeck coefficient in the grains of the material by causing additional energy filtering. Since the overall Seebeck coefficient is the weighted average of the coefficients in the grains and the grain boundaries, improving the coefficient in the grains improves the overall Seebeck coefficient.

These results indicate that it is indeed possible to nanostructure Si in a way that very high power factors can be achieved. This does not necessarily happen by utilizing low-dimensional channels, but by designing a non-uniform material geometry on the nanoscale, with a non-uniform underlying potential distribution, non-uniform dopant distribution, and non-uniform local thermal conductivity. For the figure of merit to increase, however, this needs to be combined with engineering techniques that dramatically reduce the thermal conductivity, such as introduce more disorder, or scale this geometry in a thin layer, rather than bulk-size. Individually, it seems to be possible to achieve both, high power factors and low thermal conductivities. Introducing disorder to

reduce the thermal conductivity, however, could be very detrimental for the power factor, and needs to be considered with care.

It is also worth mentioning another recent demonstration of very high TE power factors presented in Ref. [61] by Zervos *et al.* In that work, Fe₃O₄ was deposited on top of p-type Si, with the inclusion of an intermediate thin SiO₂ layer, forming an in-plane heterostructure Fe₃O₄/SiO₂/p-type Si geometry. In that experiment, contacts were placed on the Fe₃O₄ layer. At low T the structure was resistive, but for temperatures above 200K a sharp drop in the resistivity was observed due to the tunneling of carriers from the Fe₃O₄ into the accumulation layer of p-type Si. The parallel conduction hole accumulation channel offered a high electrical conductivity, whereas a large Seebeck coefficient of +1000 $\mu\text{V/K}$ was also measured at T=300K, possibly due to the fact that carriers needed to overpass the oxide in order to reach the contacts. The room temperature power factor was reported to be 70 mW/mK², an incredibly high value for Si-based structures.

Finally, an alternative geometry that has recently attracted significant attention is the nanoporous Si, or Si nanomeshes. This consists of a single-crystalline Si with embedded pores of a certain diameter, pitch, and porosity, usually placed in ordered hexagonal or rectangular arrays as shown in Fig. 1d. They are promising candidates for thermoelectric materials due to their extremely low thermal conductivity κ_l , relatively high thermoelectric power factor (bulk level), and structure stability that other nanostructured or low-dimensional systems lack [3, 5, 62, 63]. The feature sizes range from 10 to a few 100s of nanometers. These structures have thermal conductivities in the order of 1-2W/mK, and a ZT value of 0.4 was reported at 300K, one of the best values reported for Si [3]. In such geometries phonons encounter enhanced boundary scattering on the nanopore sidewalls, which results in the extremely low thermal conductivities observed, but also encounter significant coherent effects due to the specific geometry of the mesh, which changes the phonon spectrum, reduces the phonon group velocity, and drastically reduces κ_l . In a recent theoretical work, Wolf *et al.* employed semiclassical Monte Carlo simulations for phonons in Si nanomeshes in the diffusive phonon transport

limit, and compared the calculated thermal conductivity with experimental data [64]. In general, the experimental measurements showed lower conductivity compared to the semiclassical result, in some cases significantly lower, which demonstrates that indeed coherent effects could be strong. Extremely low thermal conductivities were observed for such porous structures of pore sizes from tens of nanometers down to a few nanometers, and for SiGe nanoporous material as well [65, 66, 67], indicating a possible direction for the design of a high performance Si-based TE material.

V. Conclusions

In conclusion, both theory and experiment suggests that Si can be nanoengineered to provide very large thermoelectric performance. In the past, several works demonstrated that the thermal conductivity can be reduced in the presence of lattice distortion to extremely low values, but recent works demonstrate that the power factor can also largely increase compared to bulk values. A combination of these two phenomena could provide extremely high ZT values and set the stage for Si as an effective TE material. In this review I presented results on the performance of: i) low-dimensional Si materials such as ultra-thin-layers and ultra-narrow nanowires, and ii) nanostructured Si materials. The main focus of the paper was on whether power factor improvements can be achieved. In the case of low-dimensional Si channels, it is shown that in general the power factor is lower compared to the bulk material because of increased electron-phonon scattering and surface roughness scattering, which limit the conductivity. The Seebeck coefficient does not benefit significantly by dimensionality either. In the case of nanostructured Si based channels, on the other hand, large power factors can be achieved when the underlying geometry and potential landscape are properly engineered to take advantage of energy filtering and non-uniformities in the material properties. We showed that recent studies indicated a $\sim 5\times$ improvement in the power factor of nanostructured Si compared to that of the bulk material. We have also mentioned the possibility of in-plane heterostructures such as the $\text{Fe}_3\text{O}_4/\text{SiO}_2/p$ -type Si

geometry for achieving very large power factors. Finally, we have discussed the possibility of Si nanomeshes as effective TE materials due to the potential of extremely low thermal conductivities and relatively superior structure stability.

Acknowledgements

The author would like to thank Prof. Hans Kosina, Dr. Hosein Karamitaheri, Stefanie Wolf, Prof. Dario Narducci, and Prof. Xanthippi Zianni for collaborations and various discussions.

References

- [1] A. I. Hochbaum, R. Chen, R. D. Delgado, W. Liang, E. C. Garnett, M. Najarian, A. Majumdar, and P. Yang, *Nature*, vol. 451, pp. 163–168, 2008.
- [2] A. I. Boukai, Y. Bunimovich, J. T.-Kheli, J.-K. Yu, W. A. G. III, and J. R. Heath, *Nature*, 451, 168–171, 2008.
- [3] J. Tang, H.-T. Wang, D. H. Lee, M. Fardy, Z. Huo, T. P. Russell, and P. Yang, *Nano Lett.*, 10, 10, 4279-4283, 2010.
- [4] D. Li, Y. Wu, R. Fang, P. Yang, and A. Majumdar *Appl. Phys. Lett.*, 83, 3186–3188, 2003.
- [5] K. Nielsch, J. Bachmann, J. Kimling, and H. Böttner, *Adv. Energy Mater.*, 1, 713, 2011.
- [6] G. Chen, *Semiconductors and Semimetals*, vol. 71, pp. 203–259, 2001.
- [7] R. Chen, A. I. Hochbaum, P. Murphy, J. Moore, P. Yang, and A. Majumdar, *Phys. Rev. Lett.*, vol. 101, p. 105501, 2008.
- [8] D. Li, S. T. Huxtable, A. R. Abramsin, and A. Majumdar, *Trans. of the ASME*, 127, 108–114, 2005.
- [9] P. Martin, Z. Aksamija, E. Pop, and U. Ravaioli, *Phys. Rev. Lett.*, 102, 125503, 2009.
- [10] C. J. Vineis, A. Shakouri, A. Majumdar, and M. C. Kanatzidis, *Adv. Mater.*, 22, 3970-3980, 2010.
- [11] L.D. Hicks, and M. S. Dresselhaus, *Phys. Rev. B*, vol. 47, no. 24, p. 16631, 1993.
- [12] M. Dresselhaus, G. Chen, M. Y. Tang, R. Yang, H. Lee, D. Wang, Z. Ren, J.-P. Fleurial, and P. Gagna, *Adv. Mater.*, vol. 19, pp. 1043-1053, 2007.
- [13] C. M. Jaworski, V. Kulbachinskii, and J. P. Heremans, *Phys. Rev. B*, 80, 125208, 2009.
- [14] N. Neophytou and H. Kosina, *Phys. Rev. B*, vol. 83, 245305, 2011.
- [15] N. Neophytou and H. Kosina, *J. Electronic Materials*, 41, 6, 1305-1311, 2012.
- [16] G. D. Mahan and J. O. Sofo, *Proc. Natl. Acad. Sci. USA*, vol. 93, pp. 7436-7439, 1996.

- [17] T. B. Boykin, G. Klimeck, and F. Oyafuso, *Phys. Rev. B*, vol. 69, no. 11, pp. 115201-115210, 2004.
- [18] G. Klimeck, S. Ahmed, B. Hansang, N. Kharche, S. Clark, B. Haley, S. Lee, M. Naumov, H. Ryu, F. Saied, M. Prada, M. Korkusinski, T. B. Boykin, and R. Rahman, *IEEE Trans. Electr. Dev.*, vol. 54, no. 9, pp. 2079-2089, 2007.
- [19] G. Klimeck, S. Ahmed, N. Kharche, M. Korkusinski, M. Usman, M. Prada, and T. B. Boykin, *IEEE Trans. Electr. Dev.*, vol. 54, no. 9, pp. 2090-2099, 2007.
- [20] N. Neophytou, A. Paul, M. Lundstrom, and G. Klimeck, *IEEE Trans. Electr. Dev.*, vol. 55, no. 6, pp. 1286-1297, 2008.
- [21] N. Neophytou, A. Paul, and G. Klimeck, *IEEE Trans. Nanotechnol.*, vol. 7, no. 6, pp. 710-719, 2008.
- [22] N. Neophytou, M. Wagner, H. Kosina, and S. Selberherr, *J. Electronic Materials*, 39, 9, 1902-1908, 2010.
- [23] N. Neophytou, G. Klimeck, and H. Kosina, *J. Appl. Phys.*, 109, 053721, 2011.
- [24] N. Neophytou and H. Kosina, *J. Electronic Materials*, 40, 5, 753-758, 2011.
- [25] N. Neophytou and H. Kosina, *J. Appl. Phys.*, 112, 024305, 2012.
- [26] N. Neophytou, X. Zianni, H. Kosina, S. Frabboni, B. Lorenzi, and D. Narducci, *Nanotechnology* 24, 205402, 2013.
- [27] N. Neophytou, X. Zianni, H. Kosina, S. Frabboni, B. Lorenzi, and D. Narducci, *J. of Electronic Materials*, 43, 6, 1896-1904, 2014.
- [28] R. Kim, S. Datta, and M. S. Lundstrom, *J. Appl. Phys.*, vol. 105, p. 034506, 2009.
- [29] S. Lee, F. Oyafuso, P. Von, Allmen, and G. Klimeck, *Phys. Rev. B*, vol. 69, pp. 045316-045323, 2004.
- [30] N. Neophytou and H. Kosina, *J. Computational Electronics*, 11, 1, 29-44, 2012.
- [31] N. Neophytou and H. Kosina, *Nano Lett.*, vol. 10, no. 12, pp. 4913-4919, 2010.
- [32] N. Neophytou and H. Kosina, *Phys. Rev. B*, vol. 84, p. 085313, 2011.
- [33] E. B. Ramayya, D. Vasileska, S. M. Goodnick, and I. Knezevic, *J. Appl. Phys.*, vol. 104, p. 063711, 2008.
- [34] S. Jin, M. V. Fischetti, and T. Tang, *Jour. Appl. Phys.*, 102, 83715, 2007.

- [35] M.-S. Lee and S. D. Mahanti, *Phys. Rev. B*, 85, 165149, 2012.
- [36] Q. Zhang, H. Wang, W. Liu, H. Wang, B. Yu, Q. Zhang, Z. Tian, G. Ni, S. Lee, K. Esfarjani, G. Chen, and Z. Ren, *Energy Environ. Sci.* 5, 5246, 2012.
- [37] A. Popescu and M. L. Woods, *Appl. Phys. Lett.*, 97, 052102, 2010.
- [38] H. Karamitaheri, N. Neophytou, M. Karami Taheri, R. Faez, H. Kosina, *J. Electronic Materials*, vol. 42, p. 2091, 2013.
- [39] H. Karamitaheri, N. Neophytou, and H. Kosina, *J. Appl. Phys.* 115, 024302, 2014.
- [40] Z. Aksamija and I. Knezevic, *Phys. Rev. B*, 82, 045319, 2010.
- [41] M. Luisier, *J. Appl. Phys.*, 110, 074510, 2011.
- [42] M. Luisier, *Phys. Rev. B*, vol.86, p. 245407, 2012.
- [43] D. Donadio and G. Galli, *Nano Lett.* 10, 847–851, 2010.
- [44] E. B. Ramayya, L. N. Maurer, A. H. Davoody, and I. Knezevic, *Phys. Rev. B* 86, 115328, 2012.
- [45] T. T.M. Vo, A. J. Williamson, V. Lordi, and G. Galli, *Nano Lett.*, 8, 4, pp. 1111-1114, 2008.
- [46] M. Zebarjadi, G. Joshi, G. Zhu, B. Yu, A. Minnich, Y. Lan, X. Wang, M. Dresselhaus, Z. Ren, and G. Chen, *Nano Lett.*, 11, 6, pp. 2225–2230, 2011.
- [47] B. Yu, M. Zebarjadi, H. Wang, K. Lukas, H. Wang, D. Wang, C. Opeil, M. Dresselhaus, G. Chen, and Z. Ren, *Nano Lett.*, 12, 4, pp. 2077–2082, 2012.
- [48] B. M. Curtin, E. A. Codecido, S. Krämer, and J. E. Bowers, *Nano Lett.*, 13, 11, pp. 5503–5508, 2013.
- [49] N. Neophytou and H. Kosina, *Appl. Phys. Lett.*, 105, 073119, 2014.
- [50] W. Liang, A. I. Hochbaum, M. Fardy, O. Rabin, M. Zhang and P. Yang, *Nano Lett.*, 9, 4, pp. 1689–1693, 2009.
- [51] S. Roddaro, D. Ercolani, M. A. Safeen, S. Suomalainen, F. Rosella, F. Giazotto, L. Sorba, and F. Beltram, *Nano Lett.*, 13, 3638-3642, 2013.
- [52] J. Moon, J.-H. Kim, Z. C.Y. Chen, J. Xiang, and R. Chen, *Nano Lett.*, 13, 3, pp. 1196–1202, 2013.

- [53] Y. Tian, M. R. Sakr, J. M. Kinder, D. Liang, M. J. MacDonald, R. L. J. Qiu, H.-J. Gao, and X. P. A. Gao, *Nano Lett.*, 12, 12, pp. 6492–6497, 2012.
- [54] D. Narducci, B. Lorenzi, X. Zianni, N. Neophytou, S. Frabboni, G. C. Gazzadi, A. Roncaglia, and F. Suriano, *Physica status solidi a*, 211, 6, 1255-1258, 2014.
- [55] J. Y. W. Seto, *J. Appl. Phys.*, 46, 5247, 1975.
- [56] J. W. Orton and M. J. Powell, *Rep. Prog. Phys.*, 43, 1263, 1980.
- [57] C. Jacoboni and L. Reggiani, *Rev. Mod. Phys.*, 55, 645, 1983.
- [58] <http://www.ioffe.ru/SVA/>, ‘Physical Properties of Semiconductors’
- [59] G. Masetti, M. Severi, and S. Solmi, *IEEE Trans, Electr. Dev.*, 30, 764, 1983.
- [60] B. Lorenzi, D. Narducci, R. Tonini, S. Frabboni, G.C. Gazzadi, G. Ottaviani, N. Neophytou, X. Zianni, *J. Electronic Materials*, 43, 10, 3812-3816, 2014.
- [61] M. Zervos, Z. Viskadourakis, G. Athanasopoulos, R. Flores, O. Conde, and J. Giapintzakis, *J. Appl. Physics*, 115, 033709, 2014.
- [62]. J.-K. Yu, S. Mitrovic, D. Tham, J. Varghese and J. R. Heath, *Nature Nanotechnology*, 5, 10, 718-721, 2010.
- [63] P. E. Hopkins, C. M. Reinke, M. F. Su, R. H. Olsson III, E. A. Shaner, Z. C. Leseman, J. R. Serrano, L. M. Phinney, and I. E. Kady, *Nano Lett.*, 11, 1, 107-112, 2011.
- [64] S. Wolf, N. Neophytou, and H. Kosina, *J. Appl. Phys.* 115, 204306, 2014.
- [65] J.-H. Lee, G. Galli, and J. C. Grossman, *Nano Lett.*, 8, 11, 3750-3754, 2008.
- [66] S. P. Hepplestone and G. P. Srivastava, *Phys. Rev. B*, 84, 115326, 2011.
- [67] C. Bera, N. Mingo and S. Volz, *Phys. Rev. Lett.*, 104, 115502, 2010

Figure 1:

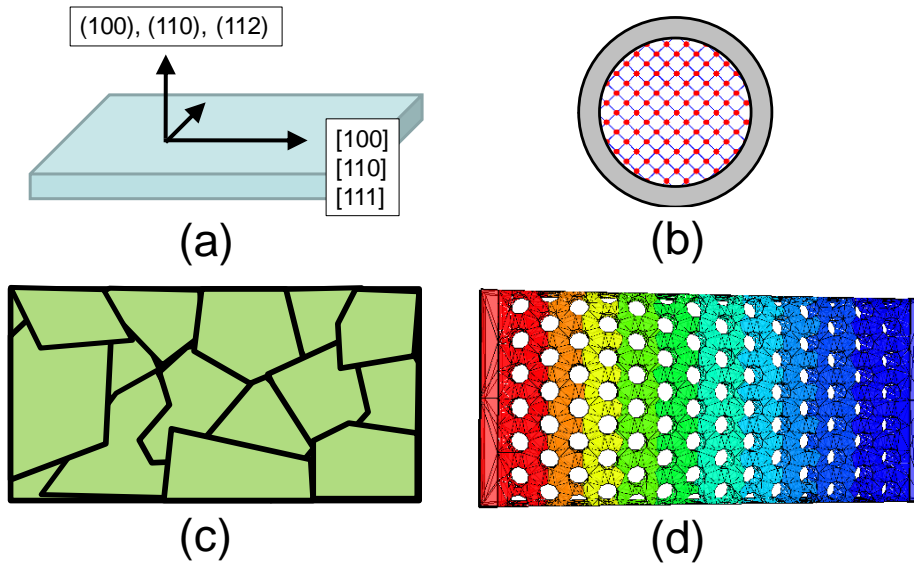


Figure 1 caption:

Si based thermoelectric materials described in this review paper. (a) Ultra-thin Si layers of various transport and confinement orientations. (b) Ultra-narrow Si nanowire. (c) Nanocrystalline Si bulk material. (d) Si nanomeshes (nanoporous material) with a temperature gradient indicated (red for hot, blue for cold).

Figure 2:

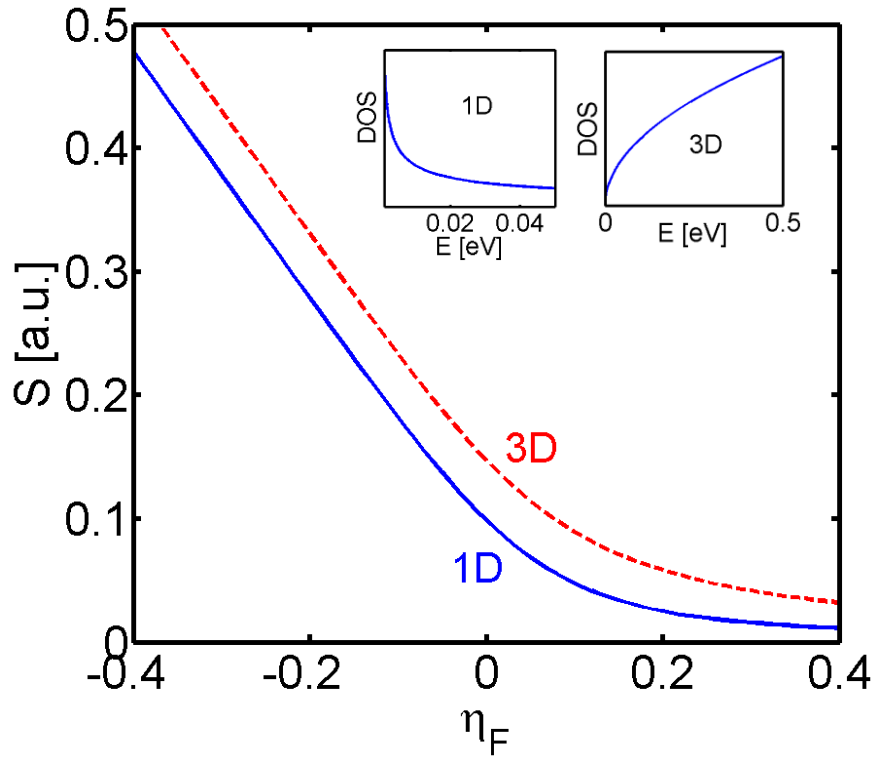


Figure 2 caption:

The Seebeck coefficient of a 3D material (red-dashed line) and of a 1D material (blue-solid line), versus the position of the Fermi level with respect to the band edge. Inset: The 1D and 3D density of states $DOS(E)$ function.

Figure 3:

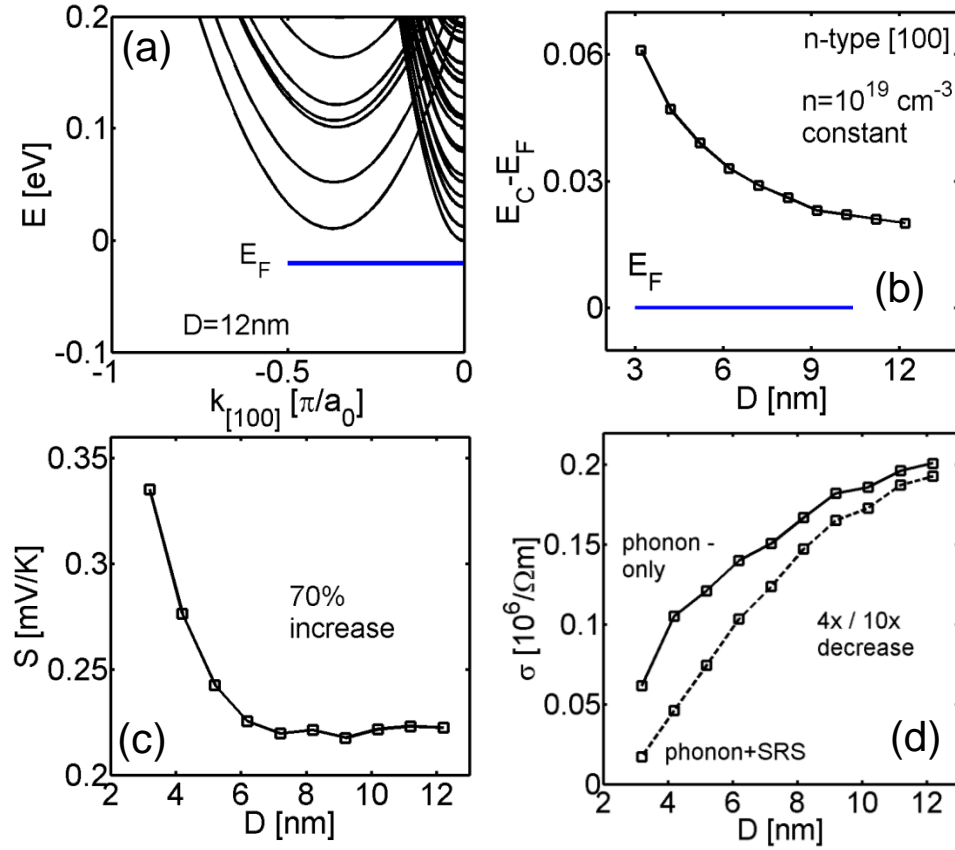


Figure 3 caption:

(a) Electronic structure for n-type [100] NW with diameter $D=12$ nm. The position of the Fermi level is noted. (b) The energy difference between the conduction band and the Fermi level in the Si nanowire channel for carrier concentration $n=10^{19}/\text{cm}^3$ versus the nanowire diameter. The position of the Fermi level is noted. (c) Seebeck coefficient and (d) electrical conductivity for the n-type [100] NW at $n=10^{19}/\text{cm}^3$ versus diameter. Solid-square lines: Only phonon scattering is considered. Dashed-square line in (d): Phonons and SRS are considered.

Figure 4:

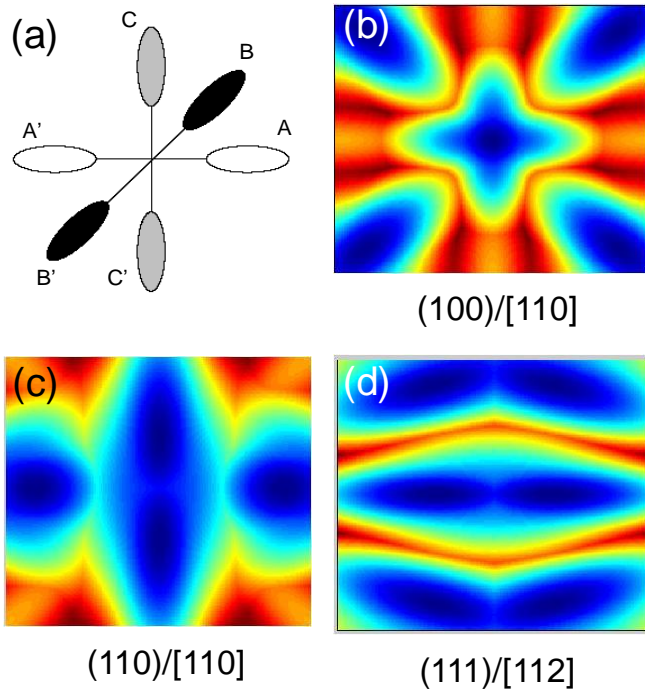


Figure 4 caption:

(a) The six energy ellipsoids of the Si bandstructure. (b-d) The 2D energy contour of the first subband of the channels on different surfaces and transport orientations (transport in the horizontal direction). The dark-blue regions are projections of the six ellipsoids onto the 2D plane. (b) The (100)/[110] channel. (c) The (110)/[110]. (d) The (111)/[112] channel.

Figure 5:

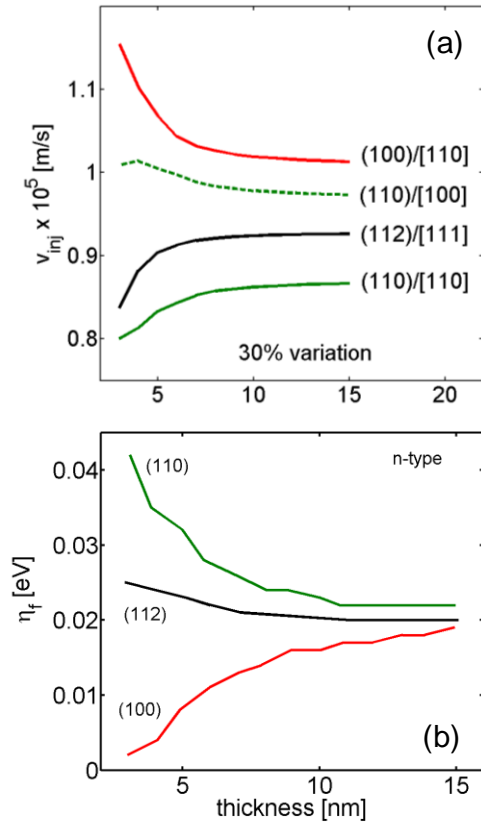


Figure 5 caption:

(a) The average ballistic injection velocity of electrons in Si UTLs with surface and transport orientations as noted, versus the layer thickness. (b) The energy difference between the conduction band and the Fermi level in the Si UTL channel for carrier concentration $n=10^{19}/\text{cm}^3$ versus the UTL thickness. Results for three channels on the (110), (112) and (100) surfaces are denoted.

Figure 6:

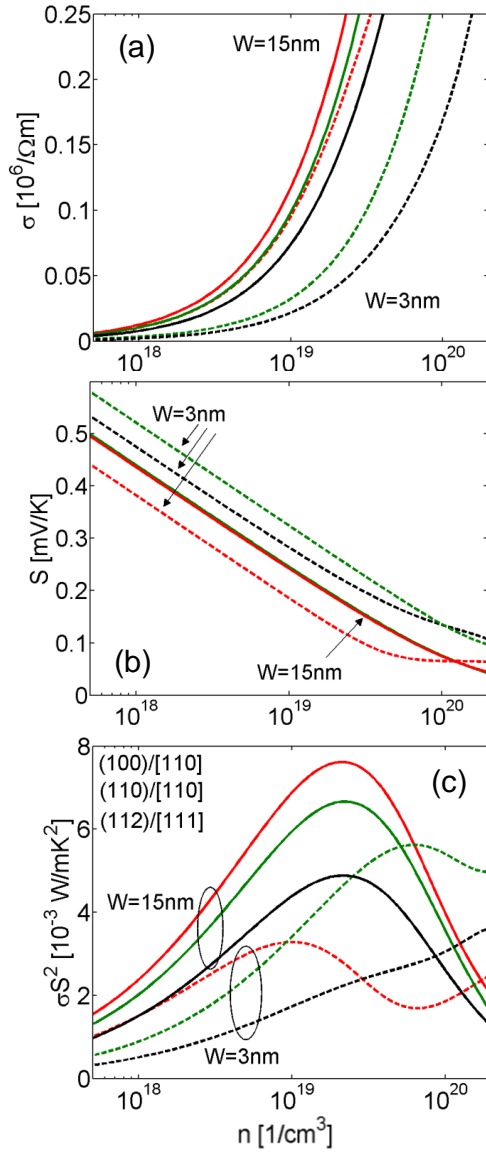


Figure 6 caption:

Thermoelectric coefficients for n-type UTLs in different confinement and transport orientations versus carrier density. Results for UTL thickness $W=15\text{nm}$ (solid lines) and $W=3\text{nm}$ (dashed lines) are presented. Channel (100)/[110] is depicted by the red lines. Channel (110)/[110] is depicted by the green lines. Channel (112)/[111] is depicted by the black lines. (a) Electrical conductivity. (b) Seebeck coefficient. (c) Power factor. Electron-phonon scattering limited transport is considered in the calculations.

Figure 7:

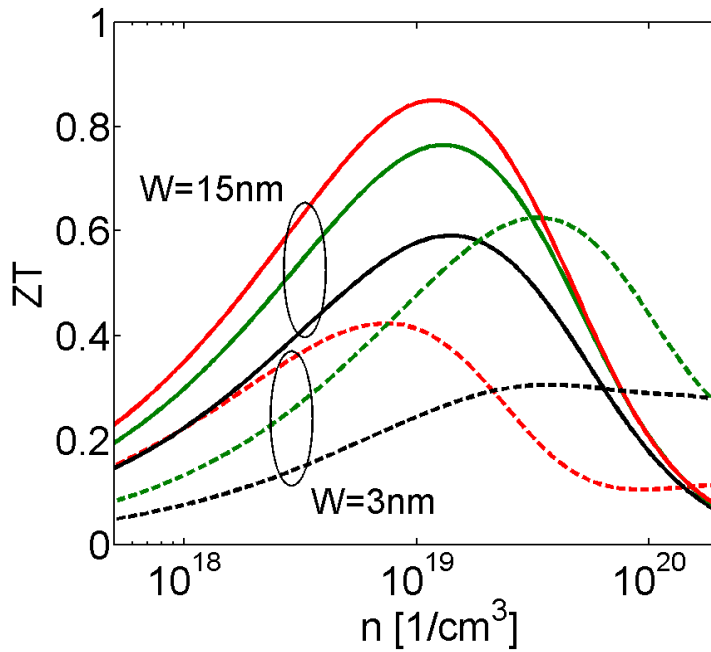


Figure 7 caption:

Thermoelectric coefficients for n-type UTLs in different confinement and transport orientations versus carrier density. Results for UTL thickness $W=15\text{nm}$ (solid lines) and $W=3\text{nm}$ (dashed lines) are presented. Channel (100)/[110] is depicted by the red lines. Channel (110)/[110] is depicted by the green lines. Channel (112)/[111] is depicted by the black lines. Electron-phonon scattering limited transport is considered in the calculations.

Figure 8:

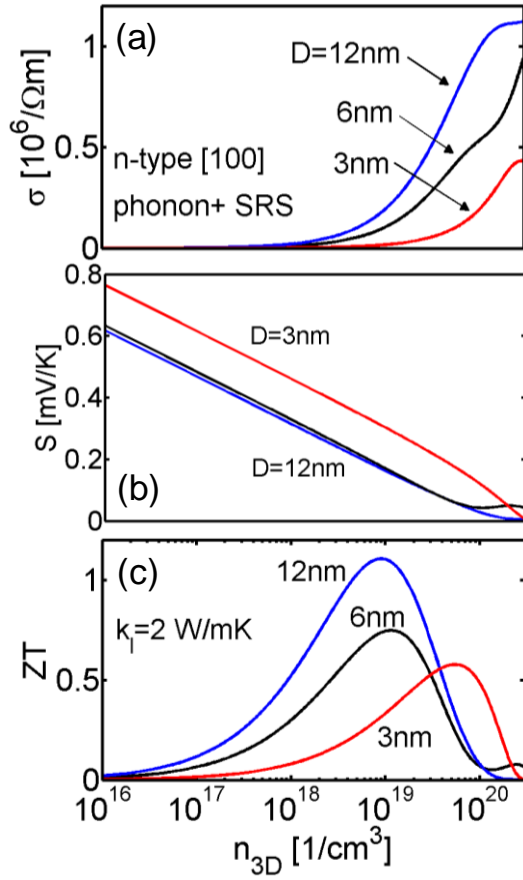


Figure 8 caption:

Thermoelectric coefficients versus carrier concentration for the n-type NW in the [100] transport orientation at 300K. NW diameters of $D=12$ nm (blue lines), $D=6$ nm (black lines) and $D=3$ nm (red lines) are depicted. Electron-phonon plus SRS limited transport conditions are considered. (a) The electrical conductivity. (b) The Seebeck coefficient. (c) The power factor.

Figure 9:

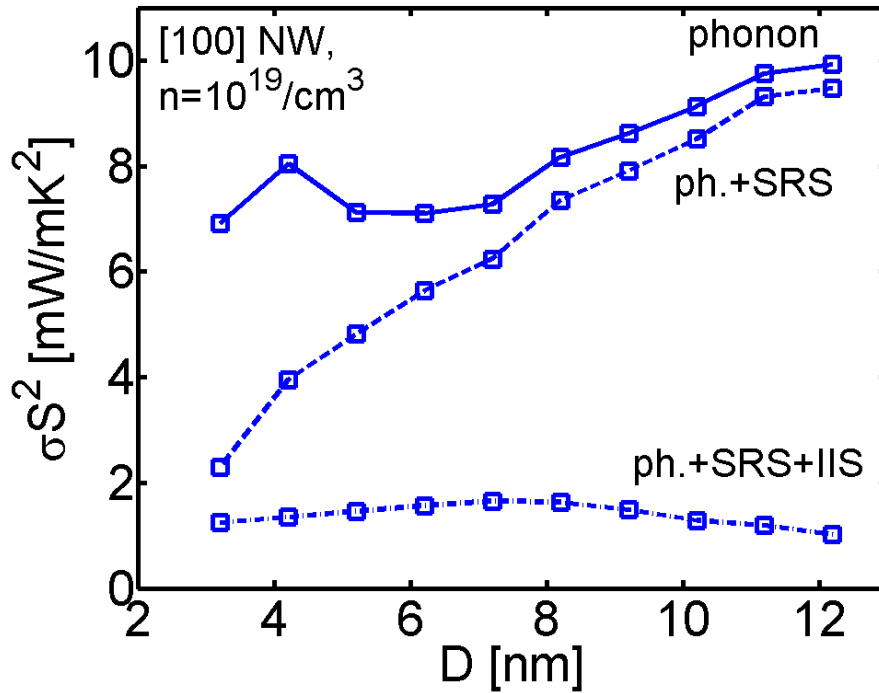


Figure 9 caption:

Thermoelectric power factor of the [100] NW at carrier concentrations of $n=10^{19}/\text{cm}^3$ versus NW diameter. Three different scattering situations are considered: i) Electron-phonon scattering limited transport (solid line). ii) Electron-phonon plus SRS scattering limited transport (dashed line). iii) Electron-phonon, plus SRS, plus ionized impurity scattering (IIS) limited transport (dashed-dotted line).

Figure 10:

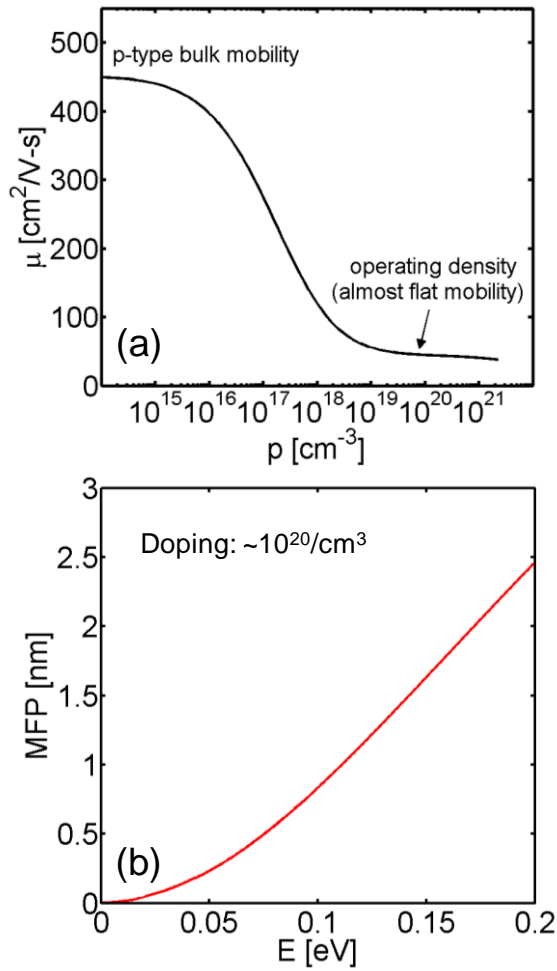


Figure 10 caption:

(b) P-type bulk Si mobility calculations. The operating region of the nanocrystalline material discussed is indicated at very high doping concentrations, where a region of almost constant ('flat' or slightly decreasing) mobility is observed. (b) The mean-free-path (MFP) for scattering at carrier concentrations $p=10^{20}/\text{cm}^3$ versus energy.

Figure 11:

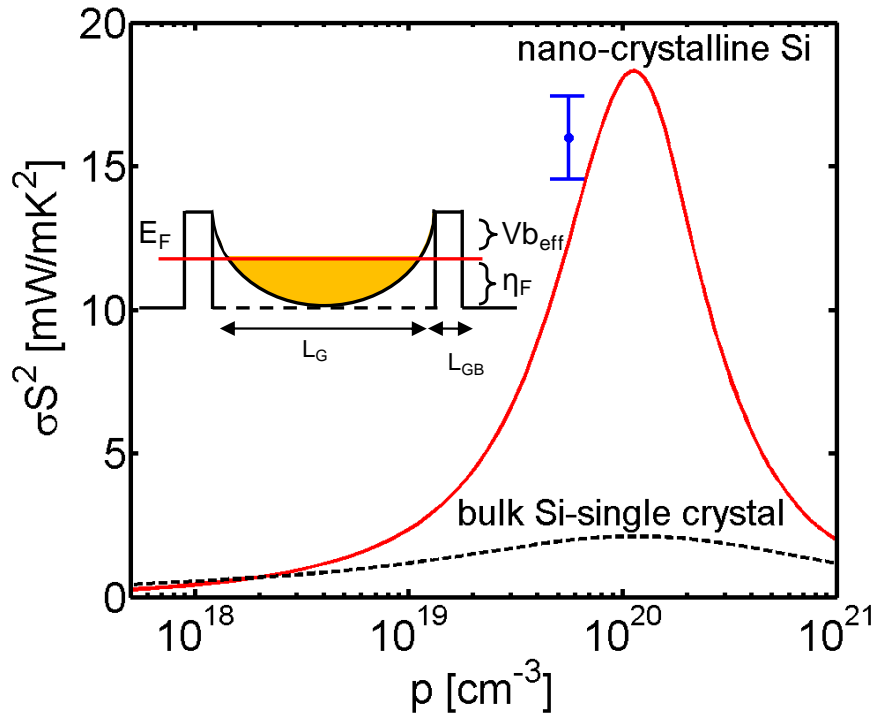


Figure 11 caption:

Simulation results for the thermoelectric power factor versus carrier concentration for p-type bulk Si (black-dashed line) and nanocrystalline Si with grain size $L_G = 30$ nm, grain boundary width $L_{GB} = 2$ nm, and barrier height $V_b = V_{b_{eff}} + \eta_F = 165$ meV (red-solid line). Measurements for the nanocomposite structure with overall concentration $p = 5.6 \times 10^{19}$ cm $^{-3}$ are indicated by the blue dots (from Ref. [26]). Inset: Schematic of the nanocomposite material grain-grain boundary geometry and underlying band edge profile. The carrier density in the material resides in the orange-colored energy region. The position of the E_F is also indicated by the red line.